Available online at www.sciencedirect.com
ScienceDirect
Acta Materialia 58 (2010) 4578–4589
Acta MATERIALIA
www.elsevier.com/locate/actamat

In situ redox cycle of a nickel–YSZ fuel cell anode in an environmental transmission electron microscope

Q. Jeangros [a], A. Faes [a,b], J.B. Wagner [c], T.W. Hansen [c], U. Aschauer [d], J. Van herle [b], A. Hessler-Wyser [a,*], R.E. Dunin-Borkowski [c]

[a] *Interdisciplinary Center for Electron Microscopy, Ecole Polytechnique Fédérale de Lausanne, CH-1015 Lausanne, Switzerland*
[b] *Laboratory of Industrial Energy Systems, Ecole Polytechnique Fédérale de Lausanne, CH-1015 Lausanne, Switzerland*
[c] *Center for Electron Nanoscopy, Technical University of Denmark, DK-2800 Kongens Lyngby, Denmark*
[d] *Chemistry Department, Princeton University, Princeton, NJ 08544, USA*

Received 15 December 2009; received in revised form 26 March 2010; accepted 10 April 2010
Available online 9 June 2010

Abstract

Environmental transmission electron microscopy is used in combination with density functional theory calculations to study the redox stability of a nickel/yttria-stabilized zirconia solid oxide fuel cell anode. The results reveal that the transfer of oxygen from NiO to yttria-stabilized zirconia triggers the reduction reaction. During Ni reoxidation, the creation of a porous structure, due to mass transport, accounts for the redox instability of the Ni-based anode. Both the expansion of NiO during a redox cycle and the presence of stress in the yttria-stabilized zirconia grains are observed directly. Besides providing an understanding of the Ni–YSZ anode redox degradation, the observations are used to propose an alternative anode design for improved redox tolerance.
© 2010 Acta Materialia Inc. Published by Elsevier Ltd. All rights reserved.

Keywords: Environmental transmission electron microscopy (ETEM); Solid oxide fuel cell (SOFC); Reduction; Oxidation; Density functional theory (DFT)

1. Introduction

Solid oxide fuel cell (SOFC) technology is a promising energy conversion option at a time when durable solutions are sought. During the electrochemical reaction of a fuel with an oxidant gas, SOFCs cogenerate heat and electricity with high efficiency [1]. Other advantages of SOFCs include flexibility of fuel use (e.g. CO, H_2 and CH_4) [2], delocalization of energy production, and reduction of pollutants such as NO_x and SO_x. The standard SOFC design is based on the use of a porous ceramic–metal (cermet) composite anode made of yttria (Y_2O_3)-stabilized zirconia (YSZ) and Ni. NiO particles are sintered with YSZ and then reduced to metallic Ni during the first operation of the cell. This reaction results in a Ni volume shrinkage of 41.6% [3], creating pores in the anode and thereby enhancing gas permeability. Although Ni-based anode-supported cells display adequate performance and steady state durability, the anode exhibits structural instability in successive redox cycles. Under normal operating conditions, fuel is supplied at the anode and Ni is kept in its reduced state. However, the Ni may reoxidize due to factors such as seal leakage, shutdown in the absence of a protecting gas or high fuel utilization. The Ni oxidation is associated with a volume expansion of 71.2% [3], which cannot be accommodated completely by the porosity created during reduction because the microstructure changes between reduction and reoxidation. Since the microstructure does not revert to the oxidized as-sintered state, stress is exerted on the YSZ matrix and cracks may appear in the thin electrolyte [3], thus degrading the performance of the cell [4]. The irreversibility of the redox cycle is poorly understood. It has been suggested that coalescence and sintering of Ni during

* Corresponding author. Tel.: +41 21 693 4830; fax: +41 21 693 4401.
E-mail address: aicha.hessler@epfl.ch (A. Hessler-Wyser).

1359-6454/$36.00 © 2010 Acta Materialia Inc. Published by Elsevier Ltd. All rights reserved.
doi:10.1016/j.actamat.2010.04.019

reduction [5–7] and the formation of porosity on reoxidation [4,8–10] may account for the instability of Ni on redox cycling. However, the reduction and oxidation processes of Ni–YSZ cermets have not previously been observed directly with nanometer spatial resolution in real time.

Environmental transmission electron microscopy (ETEM, see Fig. 1) can be used to provide dynamic *in situ* observations of chemical reactions at the nano- to micrometric scale. It allows gases at pressures up to 15 mbar to be introduced into the electron microscope column with the sample at elevated temperature and without compromising other aspects of the performance of the microscope. This technique, which has already been applied to problems in catalysis [11], semiconductor nucleation [12] and growth kinetics [13], is used here to reduce and reoxidize a 55 wt.% NiO–45 wt.% YSZ SOFC anode *in situ* to understand its redox behavior, a cause of performance degradation.

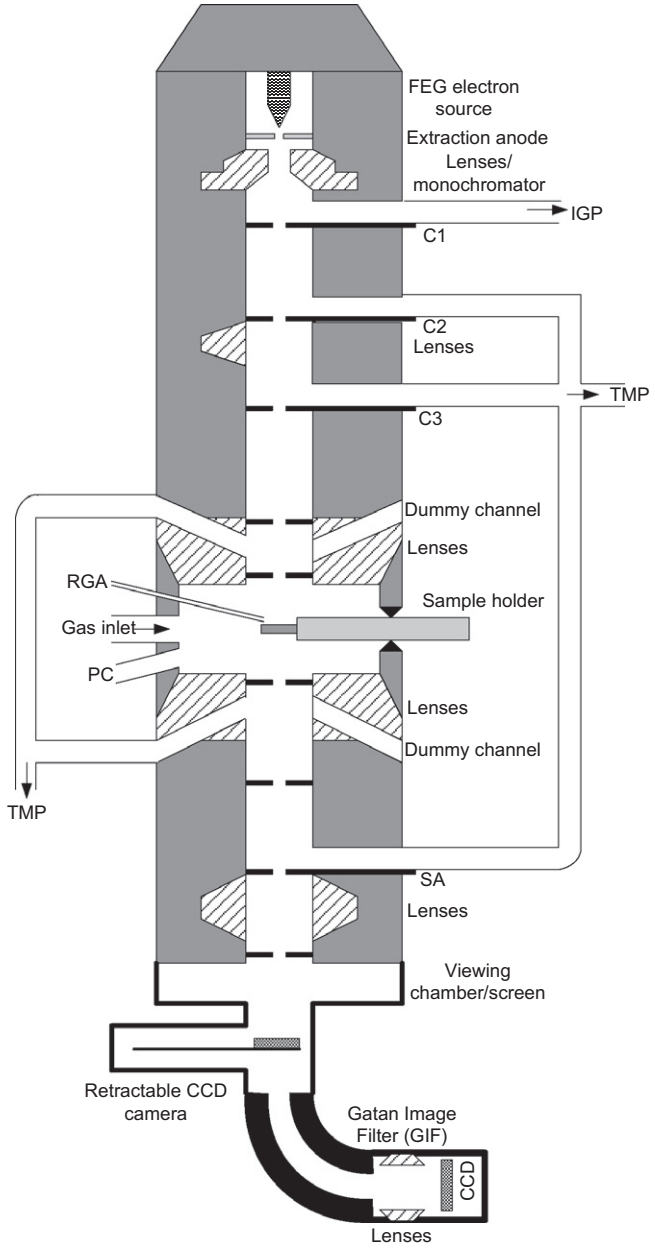

Fig. 1. Schematic diagram showing a cross-section of the components of an FEI Titan™ ETEM. Apertures, turbomolecular pumps (TMPs) and an ion getter pump (IGP) allow a gas pressure of up to ~15 mbar to be achieved at the position of the sample, while retaining an ultra-high vacuum ($<10^{-10}$ mbar) at the field emission gun (FEG) electron source. Additional components of the ETEM include a plasma cleaner (PC) and a residual gas analyzer (RGA).

2. Experimental

2.1. Electron microscopy

An anode-supported electrolyte half-cell from HTceramix SA® (Switzerland) was prepared for ETEM examination. The electrolyte was made from zirconia (ZrO_2) stabilized with 8 mol.% yttria (8YSZ), while the anode was a cermet of 55 wt.% NiO, 22.5 wt.% 3YSZ and 22.5 wt.% 8YSZ. The SOFC sample was extracted by a focused ion beam (FIB) conventional lamella lift-out method using a FEI Quanta™ equipped with an Omniprobe AutoProbe™ 100.7, welded with a platinum deposit to a stainless steel grid, and thinned down to 80 nm in a FEI Helios™. The sample was plasma cleaned for 7 min to remove any carbonaceous material.

In situ reduction and reoxidation were performed in a differentially pumped FEI Titan 80–300 ETEM with the specimen mounted in a Gatan Inconel heating holder. This configuration allows *in situ* studies in the microscope in gaseous atmospheres up to 15 mbar and at temperatures up to 1000 °C [14].

Fig. 1 shows a schematic diagram of the microscope, which includes TEM bright-field, dark-field and high-angle annular dark-field (HAADF) imaging modes, energy-dispersive X-ray (EDX) spectroscopy and elemental mapping using a Gatan image filter (GIF). Further descriptions of the ETEM technique are given in Refs. [15] and [16].

Prior to heating the sample, H_2 was introduced into the cell at a flow of 1.6 Nml min^{-1} (normal milliliters per minute, i.e. volume flow at 273 K and 101.3 kPa), corresponding to a measured pressure of 1.4 mbar at the sample. After 30 min of stabilization at 200 °C to reduce the thermal drift associated with the rapid rise of temperature, the temperature was increased to 250 °C and then to 300 °C, as no reactions occur below this temperature [6]. From this point, the sample was heated by 10 °C every 5 min up to 500 °C. At each step, bright-field images of the NiO–YSZ microstructure and diffraction patterns from one NiO grain were acquired after the sample was thermally stable (1 min after the increase in temperature). The thermal drift during these observations was limited by the small increment of temperature (10 °C), the minute of stabilization before acquiring the data and the relatively low magnification used. The zone axis was identified through comparisons with diffraction patterns simulated with the software JEMS [17]. The temperature was kept at 500 °C for 2 h and then slowly decreased to room temperature.

After the H_2 was pumped out of the environmental cell, O_2 was introduced at a flow of 1.6 Nml min^{-1}, corresponding to a measured pressure of 3.2 mbar. The temperature was increased to 200 °C and kept constant for 30 min for stabilization. The sample was then heated to 250 °C, whereupon a similar temperature ramp to that used for *in situ* reduction was started. At each step, bright-field images and diffraction patterns were acquired to study the evolution of the Ni–YSZ microstructure during reoxidation.

After reoxidation, scanning electron microscopy (SEM) in a FEI XL30 SFEG™ and FIB milling in a Zeiss NVision 40 CrossBeam™ were used to characterize the topography and the internal structure of the reoxidized NiO grains, respectively. Based on secondary electron SEM images acquired at sample tilt angles of −15°, 0° and +15°, a three-dimensional reconstruction of the topography of a Ni grain was obtained using the program MeX [18], in the form of a stereoscopic image.

2.2. Density functional theory

To confirm the reduction model proposed below, density functional theory (DFT) calculations were performed using the Quantum ESPRESSO code [19], applying the generalized gradient approximation (GGA), Perdew–Burke–Ernzerhof (PBE) exchange and correlation functional [20]. Vanderbilt Ultrasoft pseudopotentials [21] were used to describe the interaction of the Ni(3d, 4s), Y(4s, 4p, 4d, 5s), Zr(4s, 4p, 4d, 5s), O(2s, 2p) electrons with the cores. The wave functions were expanded in plane-waves up to a kinetic energy cut-off of 50 Ry, while using 500 Ry for the augmented density. The large simulation cell size allowed reciprocal space sampling to be restricted to the gamma point.

The simulation cell for the YSZ–NiO interface was constructed by putting a 6 Å thick (1 0 0) slab of NiO (lateral dimensions 8.3 × 8.3 Å) on top of a 5.5 Å thick (1 1 0) slab of cubic ZrO_2 (lateral dimensions: 10.1 × 14.3 Å), which contained two Y atoms at the interface (effective concentration 6.67%), while keeping the topmost NiO and bottommost ZrO_2 layer fixed. The accumulation of Y at the interface is justified due to segregation resulting from ionic radii mismatch between Y (0.90 Å) and Zr (0.72 Å). As a detailed study of the Y distribution around the interface was beyond the scope of the present work, the two Y atoms were placed in the same row in the interface plane. This is reasonable as previous work demonstrated the existence of yttrium in this pair configuration [22]. It should also be noted that while in this setup the periodicity of NiO is not preserved parallel to the interface plane, the inner part of the resulting interface retains the desired structure as indicated by limited relaxations in this zone. After complete relaxation (forces $< 10^{-3}$ a.u. $= 0.05$ eV $Å^{-1}$), vacancies were created close to the interface in both parts and a nudged elastic band (NEB) calculation [23] run between these two states, keeping the same atoms fixed as during relaxation.

3. Results

3.1. In situ reduction

A sequence of bright-field TEM images, which reveal the evolution of the microstructure in the specimen during *in situ* reduction, is shown in Fig. 2 (see also Supplementary Video 1). Fig. 2a shows the as-sintered microstructure at 300 °C and time zero, with a Ni elemental map shown as an inset in the top right corner and a [0 1 2] diffraction pattern from one NiO grain in the top left corner. The inhomogeneous contrast of the Ni map could be due to the irregular thickness of the TEM lamella and possible superposition of Ni and YSZ. FIB preparation of porous materials induces a curtaining effect during ion milling, giving samples that are not perfectly plane-parallel. Nanoporosity is observed to form in the NiO grains to accommodate the volume shrinkage that results from the reduction of NiO to Ni. As seen more clearly in Supplementary Video, small nanovoids are first observed at 340 °C at NiO/YSZ interfaces: the interface appears irregular with blurred white spots (indicated by arrows in Fig. 2b). The pores are seen more clearly in Fig. 2c (indicated by arrows) as they grow and form closer to the centers of NiO grains at higher temperature. The NiO becomes depleted in oxygen behind the porosity front. When the temperature reaches 420 °C, the NiO free surface is reduced directly, and porosity forms uniformly across the NiO grains (Fig. 2d). Pores are observed at NiO/NiO grain boundaries only when the free surface reduction has started. At these temperatures, coalescence of the porosity during the temperature ramp is observed to result from reduction and not from Ni reorganization (Fig. 2e and f).

NiO and Ni are both cubic with lattice parameters of 0.418 and 0.368 nm, respectively. Both the additional reflections and the satellite spots that are observed in the diffraction patterns in Fig. 2d,e and f indicate that the Ni grows coherently on its oxide, with the same crystallographic orientation after reduction (see Supplementary Video 2). The diffraction pattern acquired at 500 °C shows that NiO is still present in the grains, although the intensity of the NiO satellite spots has decreased (Fig. 2f).

In addition, particles only a few nanometers in diameter are observed in large numbers across and around Ni grains after reduction. Electron energy-loss spectroscopy of particles located away from the bulk Ni grains revealed that they are pure Ni.

3.2. In situ reoxidation

Fig. 3 shows a sequence of bright-field images illustrating the *in situ* reoxidation of the Ni–YSZ composite anode (see Supplementary Video 3). With increasing temperature, the nanoporosity that was created during *in situ* reduction is filled by NiO (Fig. 3a,c and e and Supplementary Video 4). In contrast to the reduction process, which started at the NiO/YSZ interfaces, reoxidation occurs uniformly over the Ni surface.

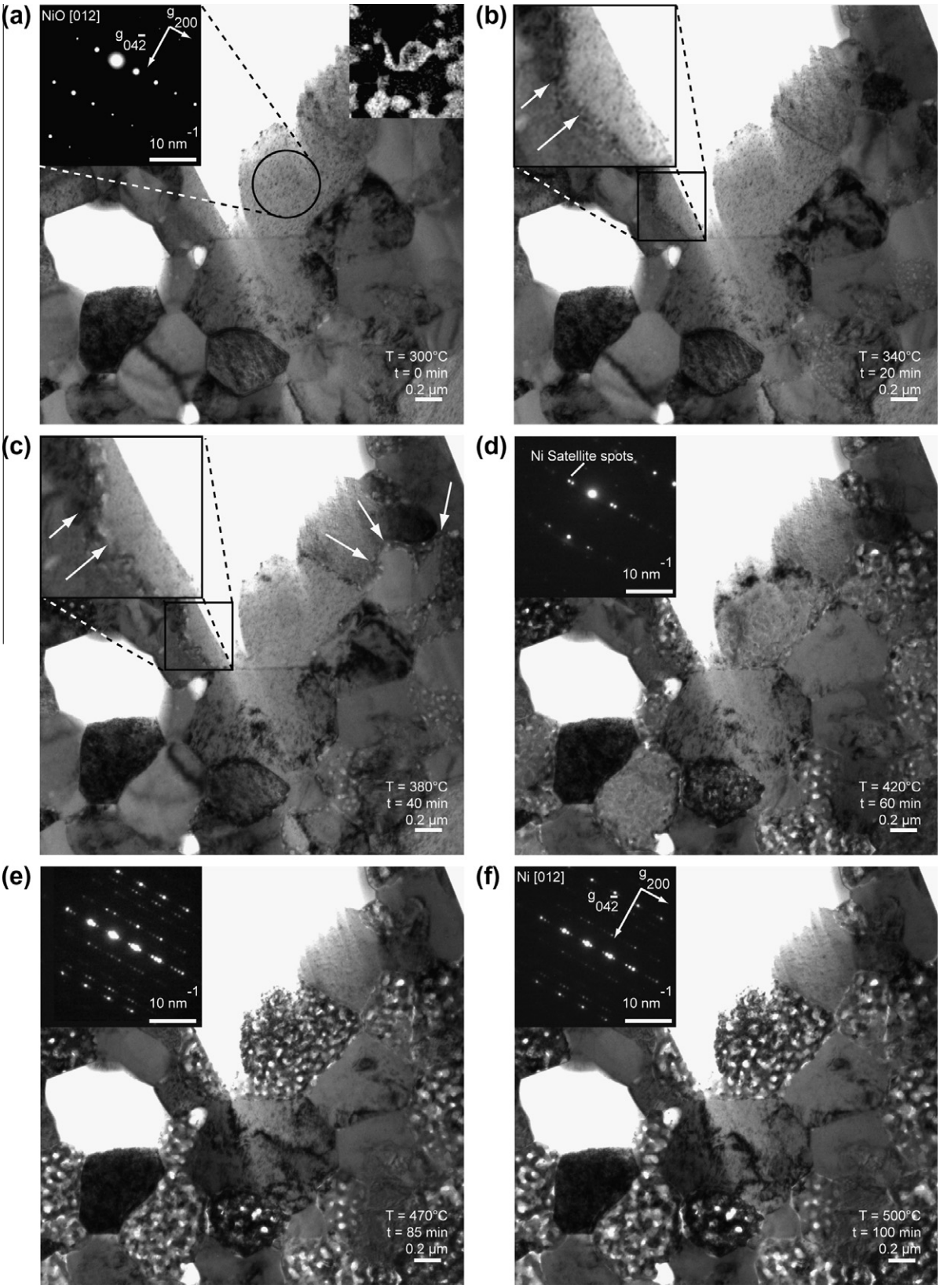

Fig. 2. Bright-field TEM images acquired during *in situ* reduction of a NiO–YSZ anode precursor in 1.4 mbar of H_2. Higher magnification images, diffraction patterns and a nickel map obtained using energy-filtered TEM are shown as insets. The arrows in (b) and (c) show the nanovoids.

Fig. 3 shows that the NiO that forms during reoxidation is polycrystalline, with diffraction rings first appearing at ~290 °C and becoming more clearly visible above 310 °C (Fig. 3b and Supplementary Video 5).

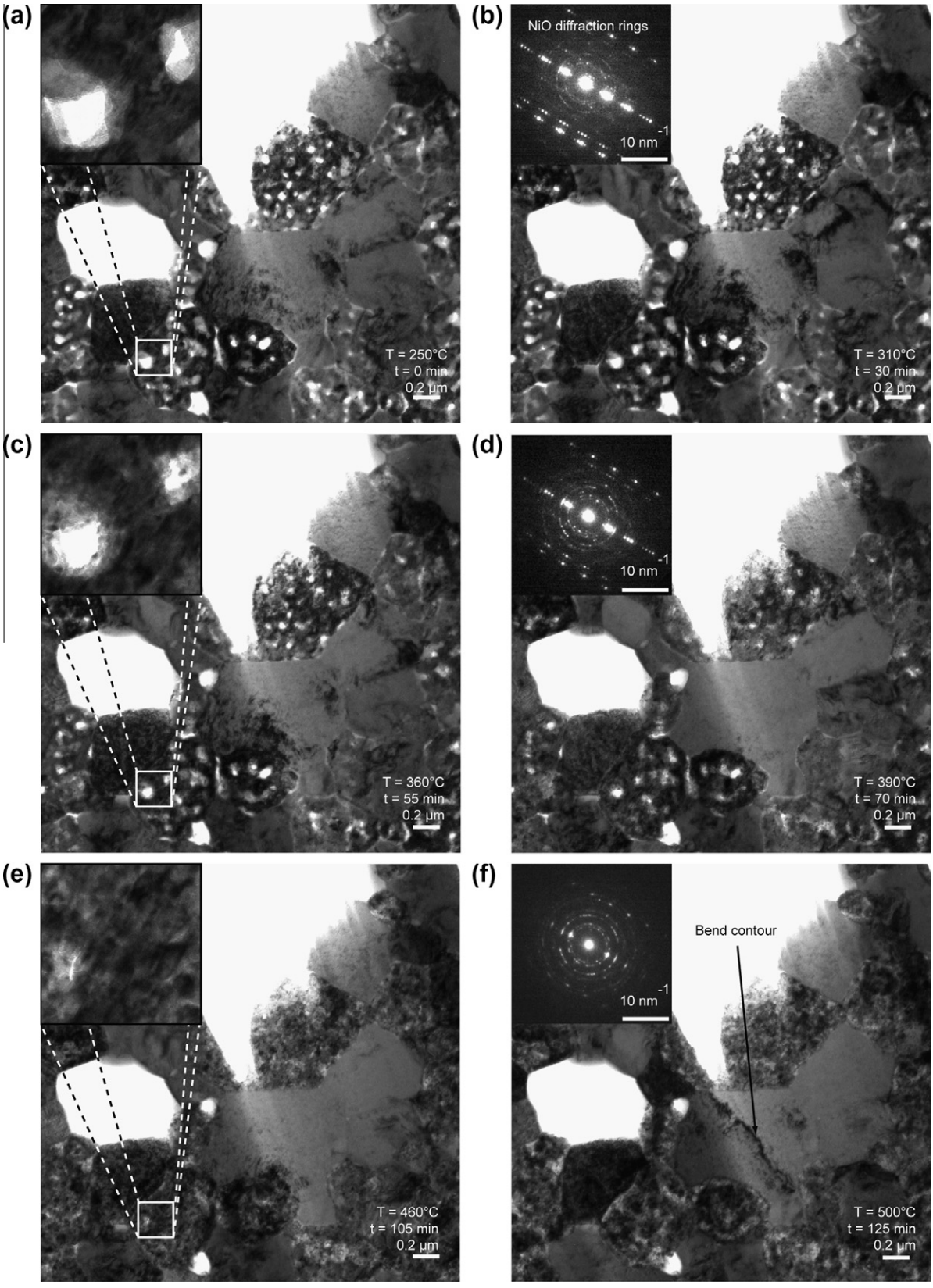

Fig. 3. Bright-field TEM images acquired during *in situ* reoxidation in 3.2 mbar O_2. Higher magnification images and diffraction patterns are shown as insets.

Fig. 4 shows further images of the microstructure, from which it is clear that the reoxidized NiO exhibits a significantly more inhomogeneous structure than the as-sintered grains (compare Figs. 2a and 3f). Whereas the

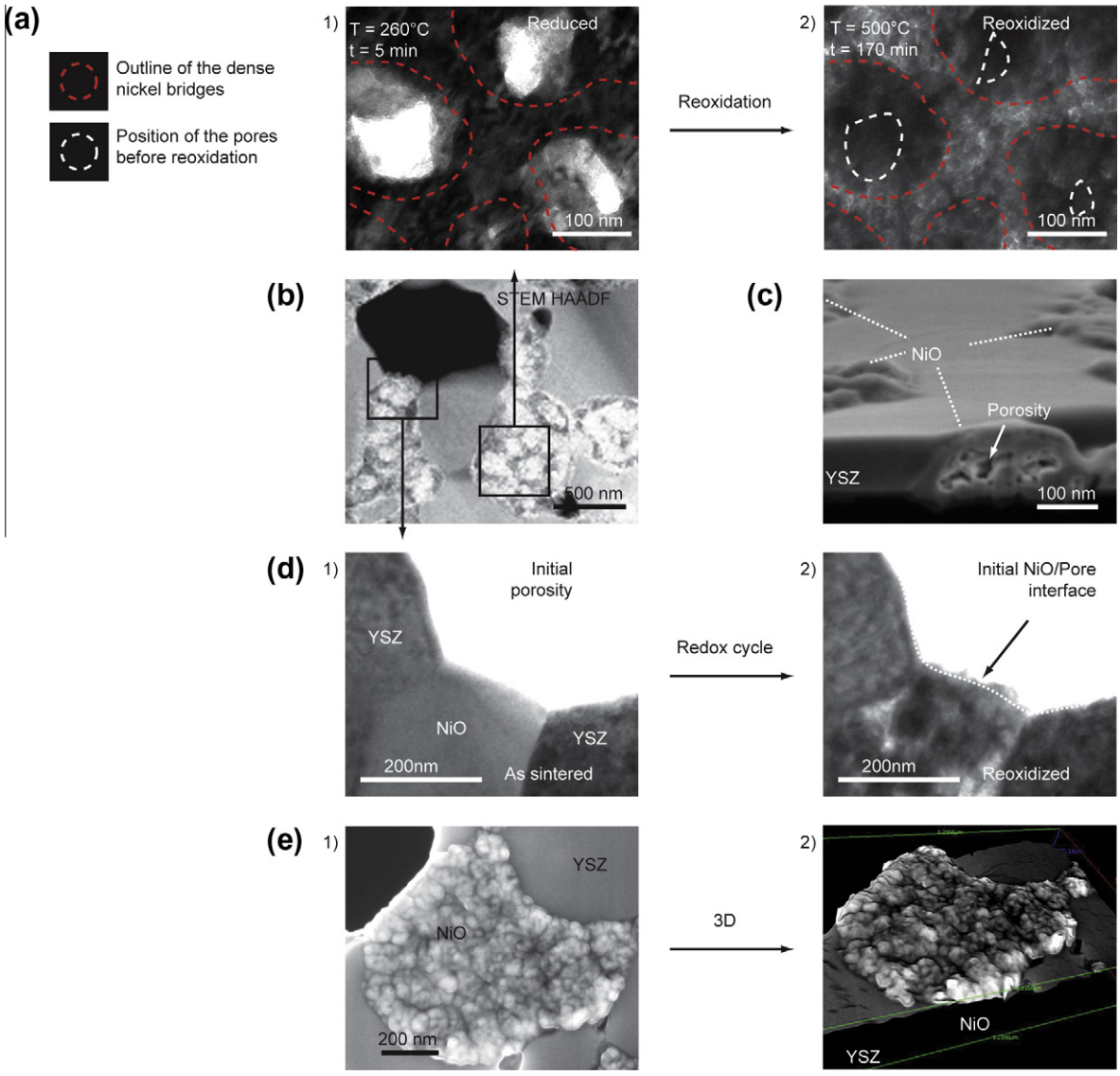

Fig. 4. Microstructural observations leading to a reoxidation model. (a) Bright-field images illustrating the transfer of atoms from the initially dense Ni to the intragranular porosity. (b) Corresponding HAADF image. (c) SEM image of pores created during reoxidation. (d) BF TEM images illustrating the expansion of Ni into as-sintered pores following a redox cycle. (e) SEM secondary electron image and three-dimensional reconstruction of the topography of a NiO grain.

reduced Ni formed a network of bridges surrounding pores (Fig. 4a.1), the pores became filled after *in situ* reoxidation (Fig. 4a.2). The HAADF image shown in Fig. 4b demonstrates the presence of less dense (darker) NiO areas at the former positions of the Ni bridges.

The presence of internal porosity in the reoxidized Ni is confirmed by secondary electron SEM images of FIB-milled cross-sections (Fig. 4c), in which partially interconnected pores that are ~50 nm in size are observed in the reoxidized Ni.

Ni expands on reoxidation, not only into the original pores (Fig. 4d.1 and d.2) but also out of the sample plane, as shown using SEM followed by three-dimensional reconstruction of the topography of the sample surface (Fig. 4e.1 and e.2).

4. Discussion

4.1. In situ reduction

The *in situ* reduction observations showed that the transformation of NiO grains into metallic Ni is coherent with the original phase. This observation was already reported by Waldbillig et al. [4], who also observed satellite spots when they examined a TEM sample that had been reduced *ex situ* at 700 °C. Dickey et al. [24] studied the reduction of the NiO/YSZ interface and also reported the epitaxial growth of Ni on NiO. Such an epitaxial relationship may be lost as the thickness of the Ni layer increases [25,26].

Ni nanoparticles have been observed. Their origin could be from FIB milling during TEM sample preparation. However, the Ni nanoparticles are not present on YSZ grains after reduction, and therefore likely formed as part of the reduction process, when Ni clusters became surrounded by voids and isolated from the bulk Ni grains [26]. The formation of such Ni nanoparticles at the surface of the metallic phase could be beneficial for fuel cell performance. At standard operating temperature, these nanoparticles are normally not stable due to coarsening of the Ni phase [27,28], but they influence the initial transient performance of the fuel cell. Such results illustrate the complexity of the dynamic evolution of the microstructure, which has previously been observed in a TEM specimen only following *ex situ* reduction [4].

The microstructural observations are summarized schematically in Fig. 5a, which shows (1) NiO/YSZ interface reduction at 340 °C (corresponding to Fig. 2b) and (2) NiO free surface reduction at 420 °C (corresponding to Fig. 2d). The high ionic conductivity of YSZ enhances interfacial phase transformations [29]. Dickey et al. [24] reduced a NiO–ZrO_2 composite anode *in situ* using a 100 kV focused electron probe and observed the start of the reaction at the NiO/YSZ interface, where oxygen was removed from the NiO through the conductive YSZ. In the present experiments, oxygen ions from NiO are likely to move to the oxygen vacancies that are inherently present in the ion-conducting YSZ at 340 °C, as shown in Fig. 5b.1 for the interfacial atomic structure proposed by Dickey et al. [24]. Indeed, the NEB calculation (Fig. 6) clearly shows that the relative defect energy is much lower when oxygen is in the YSZ part, which translates to the vacancy being in the NiO part of the interface. As electrostatics cannot account for this decrease in energy, improved misfit strain relaxation with the vacancy in NiO is likely as the origin of this energy difference. The relatively large energy difference indicates that the population of vacancies close to the interface in the YSZ part should be negligible. Although this is clearly only a single model interface, the magnitude of the result provides the assurance that results should be similar for other possible interface structures. When the oxygen ions reach the YSZ surface, they react with hydrogen and are desorbed as water (Fig. 5b.2 and b.3). Shishkin and Ziegler [30] used *ab initio* periodic calculations based on DFT to demonstrate that H_2 adsorption, dissociation and desorption are energetically favorable (exothermic) on YSZ, on which vacant sites are filled by externally provided oxygen atoms. Following the work of Bonvalot-Dubois et al. [31], we propose that two separate reactions can be used to describe the transfer of oxygen ions from NiO to YSZ and subsequent water desorption.

At the inner YSZ/NiO interface:

$$O_O(\mathrm{NiO}) + V_O^{\cdot\cdot}(\mathrm{YSZ}) \rightarrow O_O(\mathrm{YSZ}) + V_O^{\cdot\cdot}(\mathrm{NiO}) \quad (1)$$

where O_O(NiO) is an oxygen ion in NiO, $V_O^{\cdot\cdot}$(YSZ) is an oxygen vacancy in YSZ, O_O(YSZ) is an oxygen ion in YSZ and $V_O^{\cdot\cdot}$(NiO) is an oxygen vacancy in NiO. Subsequently, at the NiO/YSZ/gas interface:

$$H_2 + O_O(\mathrm{YSZ}) \rightarrow H_2O(g) + V_O^{\cdot\cdot}(\mathrm{YSZ}) + 2e^-(\mathrm{NiO}) \quad (2)$$

The creation of surface oxygen vacancies in NiO activates another mechanism: the adsorption of H_2 on Ni atoms adjacent to oxygen vacancies (Fig. 5b.4). Rodriguez et al. [32] used first-principles DFT calculations to show that the adsorption and dissociation of hydrogen molecules, and therefore the reduction of NiO by desorption of water, are favored at such sites when compared with reduction on a defect-free surface (Fig. 5b.5). Ni clusters are created at the NiO/YSZ interface as oxygen is removed (Fig. 5b.6). An oxygen elemental map acquired from a similar sample that had been reduced in the ETEM under the same conditions demonstrates that oxygen is depleted from the interface (see Fig. 7a) and therefore that oxygen is desorbed as H_2O directly at the NiO/Ni interface rather than transferred to the YSZ. The resulting vacancies in the NiO allow reduction to continue towards the center of the grain, by enhancing the adsorption and dissociation of hydrogen on Ni atoms adjacent to the oxygen vacancies. Reduction is therefore autocatalytic, as oxygen atoms are removed as the reaction proceeds, increasing the number of adsorption sites.

It has previously been established using different techniques [32–34] that the time for Ni to nucleate on NiO depends on the generation of oxygen surface vacancies. Here, at 420 °C, a sufficient number of oxygen surface defects is present to trigger direct reduction of the free surface (as in Fig. 5b.4–b.6, but in the absence of YSZ).

4.2. In situ reoxidation

The *in situ* reoxidation observations corroborate the *ex situ* observations on a TEM lamella made by Waldbillig et al. [4]. Indeed, these authors observed similar polycrystalline diffraction rings after *ex situ* reoxidation of a NiO–YSZ TEM sample, and suggested that the intragranular pores that form on reduction provide sites at which NiO can nucleate in different orientations. The reoxidation mechanism that is proposed below is also likely to explain the polycrystalline growth of reoxidized Ni [35]. The presence of Ni nanoparticles after *in situ* reduction may also contribute to the polycrystalline structure observed after reoxidation.

Based on the present observations and on previously published work [35–37], a model for Ni reoxidation in the ETEM is proposed (Fig. 8). Oxygen molecules are first adsorbed, dissociated and ionized. The resulting oxide nuclei grow laterally until impingement occurs. The dominant mass-transport mechanism at these temperatures (300–500 °C) is known to be the outward diffusion of Ni ions along oxide grain boundaries and dislocations [35–37] through the oxide layer to the surface where they react with oxygen (Fig. 8.1). This process leaves vacancies at the NiO/Ni interface (Fig. 8.2). Either the oxide layer

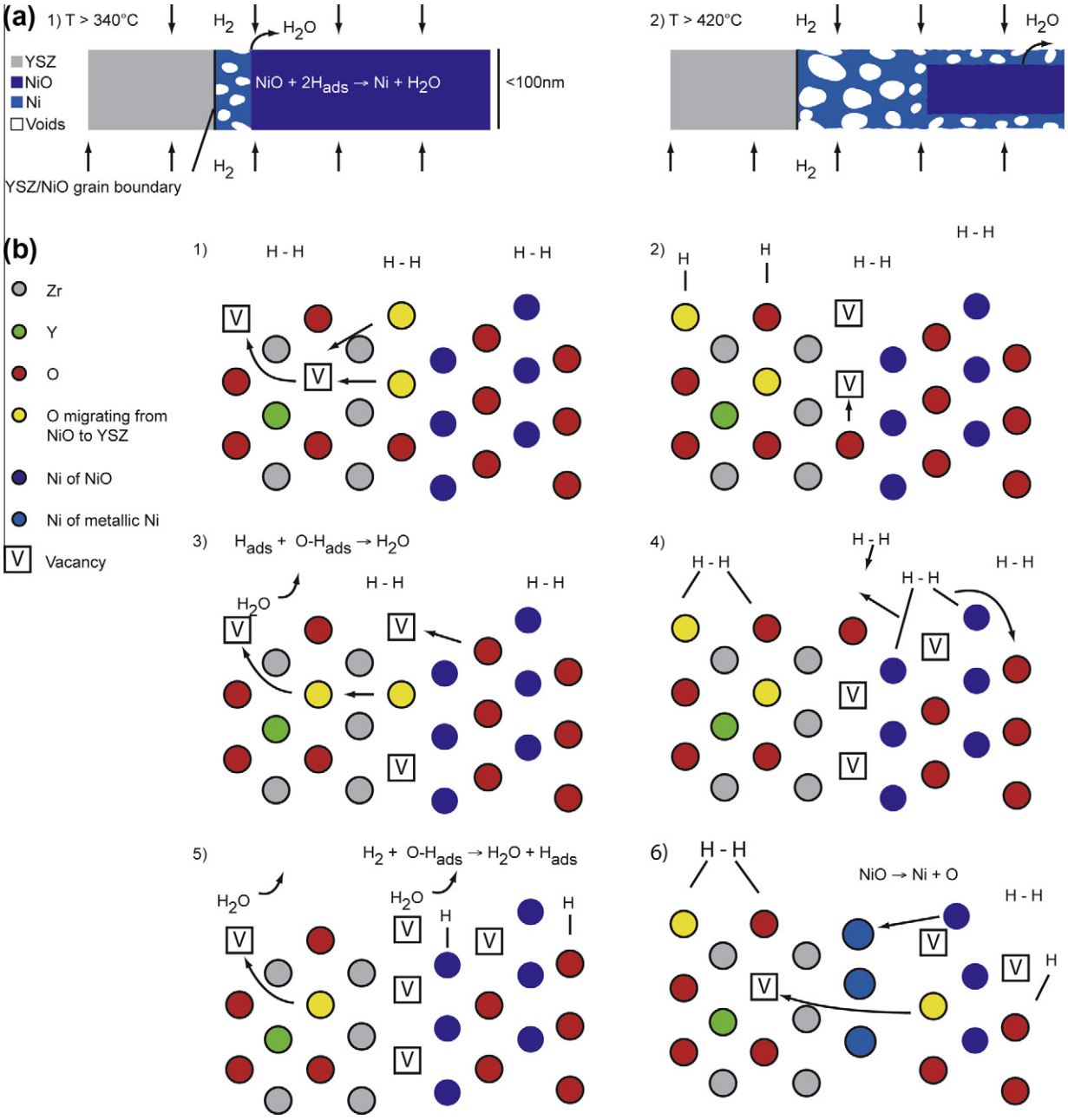

Fig. 5. Schematic diagrams describing the proposed mechanism of NiO reduction. (a) Reduction starts at 340 °C at the NiO/YSZ interface and proceeds from the free NiO surface above 420 °C. (b) Atomic model of the interface based on the work of Dickey et al. [24] illustrating: (1) the transfer of oxygen from NiO to the YSZ vacant sites; (2) dissociative adsorption of H_2 on surface oxygen atoms on the YSZ structure; (3) desorption of water; (4) dissociative adsorption of H_2 on Ni atoms adjacent to oxygen vacancies; (5) transfer of adsorbed hydrogen and desorption of water; (6) creation of Ni nuclei at the interface with YSZ.

thickens or a new oxide film grows at the grain boundary. As Ni^{2+} is transported from the interface, the vacancies coalesce to form voids at the Ni/NiO interface (Fig. 8.3). This outward mass transport is not balanced by inward growth of NiO, as the inward oxygen diffusion speed along the grain boundaries and through the lattice is several orders of magnitude lower at these temperatures [35]. Fig. 8.4 shows a schematic diagram of two regions of Ni surrounding an intragranular pore created during reduction. Outward mass transport leaves holes at the position of the Ni (Fig. 8.4 and 8.5). When a Ni particle is reoxidized, a pore is left at its position inside a NiO shell if the interface cannot recess inwards (Fig. 8.6). The presence of neighboring YSZ grains constrains the expansion of NiO in the specimen plane, while the sample is free to expand out of the plane. Similar pores inside NiO grains were observed by Faes et al. [3] in FIB-prepared cross-sections of a bulk anode that had undergone a redox cycle

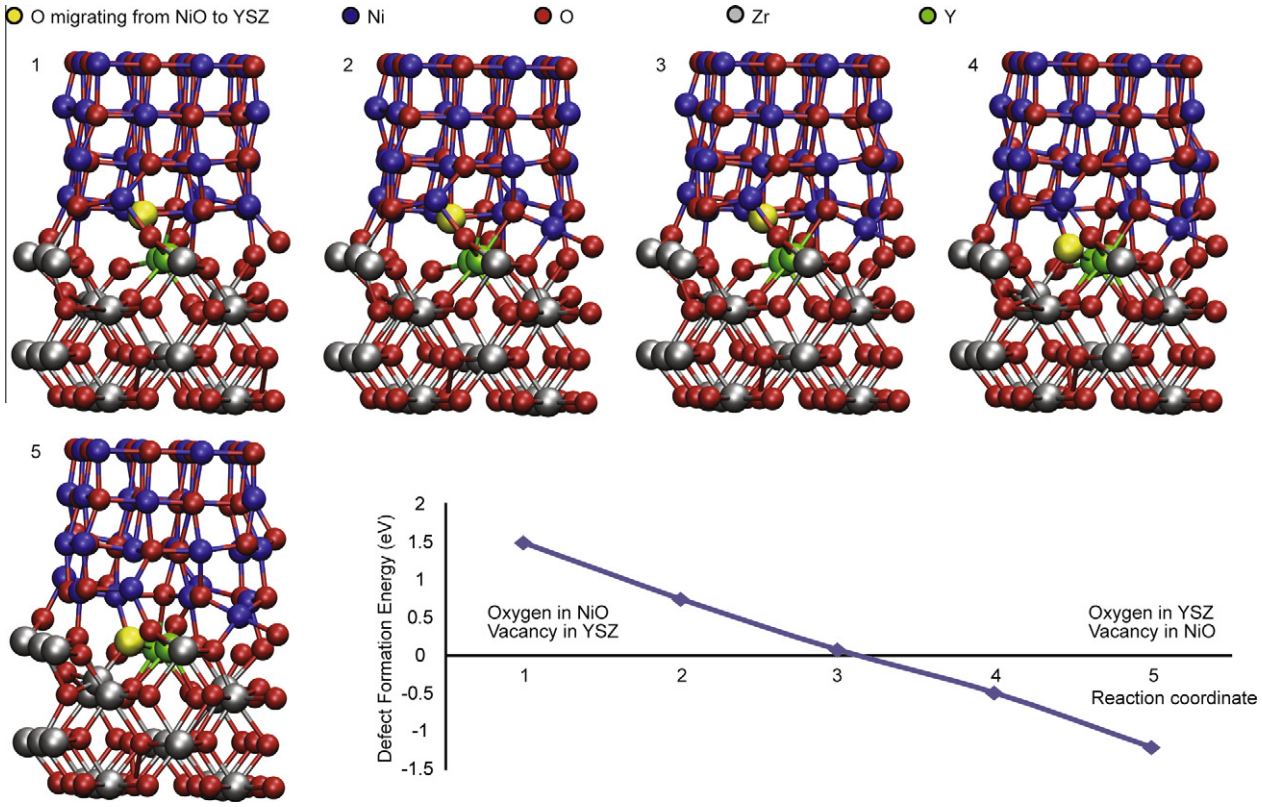

Fig. 6. Nudged elastic band calculations to determine the formation energy of an oxygen defect along the NiO/YSZ interface.

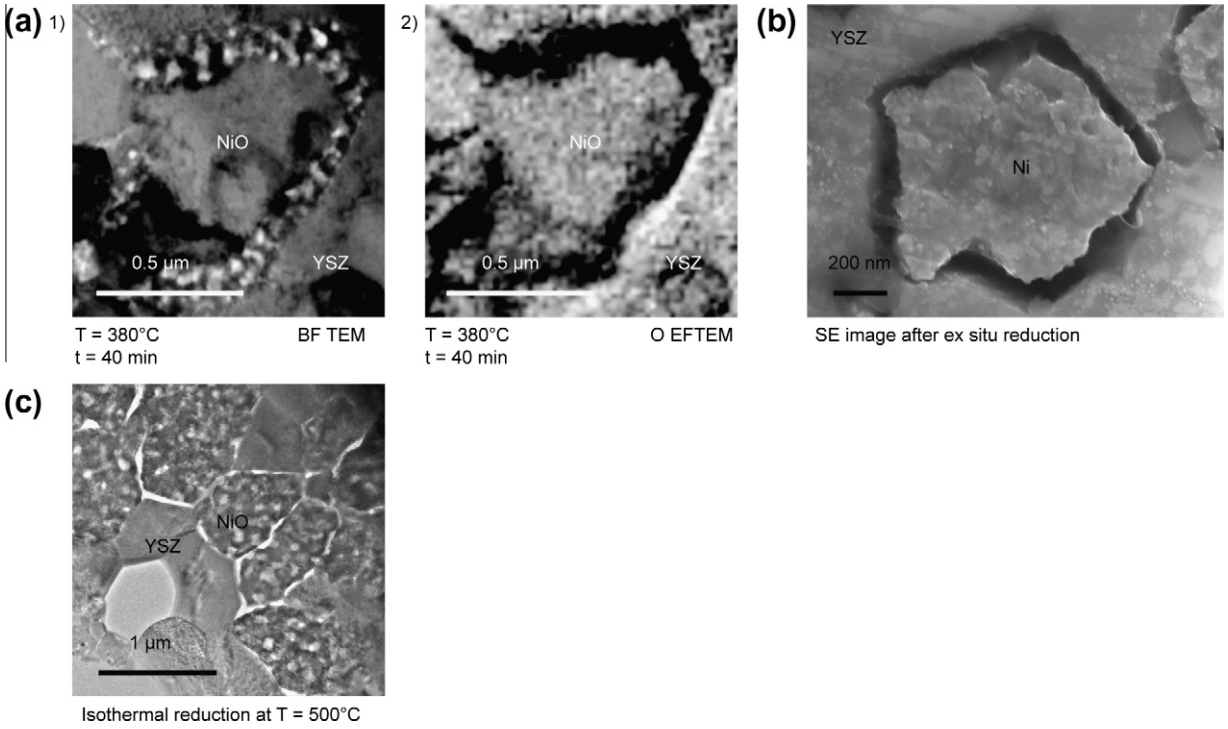

Fig. 7. Additional reduction observations. (a) BF TEM image and oxygen elemental map (O EFTEM) of the NiO/YSZ interface acquired at 380 °C (different NiO–YSZ sample). (b) SE image of a bulk sample reduced *ex situ* using the same temperature ramp as the TEM sample. (c) TEM image showing NiO/YSZ voids after isothermal reduction at 500 °C in the ETEM (different NiO–YSZ sample).

at 550 °C. Even if the expansion of NiO is constrained in three dimensions by the YSZ backbone, pores are still created by the outward diffusion of Ni ions, as in the present thin TEM sample.

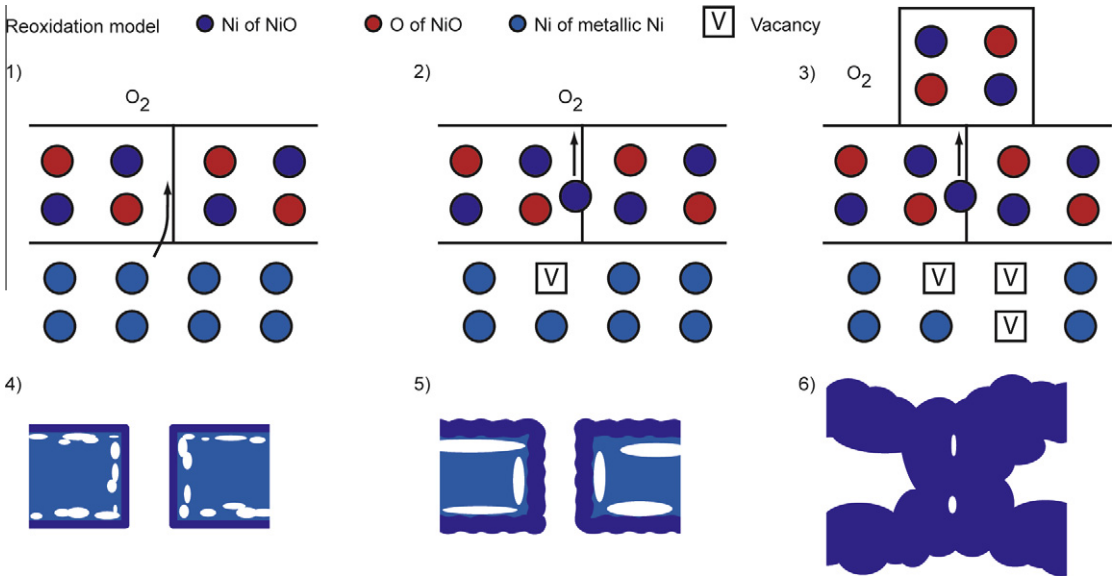

Fig. 8. Proposed reoxidation model describing the outward diffusion of Ni along grain boundaries/dislocations to create a porous structure.

4.3. ETEM factors

Factors that include TEM specimen preparation, sample geometry and the presence of the high-energy electron beam can all affect ETEM observations. Although FIB sample preparation is known to result in gallium implantation and the formation of an amorphous layer on the specimen surface [38], both effects are likely to be reduced by heating the sample in the ETEM, which results in recrystallization of the sample surface. Areas of the specimen that were exposed to the electron beam were observed to be reduced faster, presumably due to a combination of heating, desorption of oxygen due to electron impact on the specimen surface [39,40] and ionization of the molecular hydrogen gas by the electron beam, which changes the adsorption energy of hydrogen. Although a 100 kV focused electron probe has previously been observed to reduce NiO to Ni *in situ* at a NiO/c-ZrO_2 interface without the presence of fuel [24], we did not observe such a phenomenon, presumably because the as-sintered microstructure was imaged in TEM mode, i.e. with a smaller dose per unit area. In the presence of soft carbon species, the reduction of NiO can occur spontaneously in a TEM [25]. However, in our case, the sample was plasma cleaned for 7 min prior to reduction, thereby limiting or suppressing the presence of carbonaceous species on its surface.

Scanning electron microscopy does not reveal the presence of nanovoids in Ni grains of bulk samples reduced under similar conditions as the ETEM sample (Fig. 7b). The presence of nanopores is probably caused by the extreme thinness of the TEM lamella (80 nm); small irregularities in the reaction front will lead to the formation of nanopores on the surface or be trapped in the Ni/NiO grains, which are seen directly by TEM. As the reduction reaction continues, those pores will grow and coalesce into bigger pores, which will eventually go through the thin TEM sample. Waldbillig et al. [4] reduced a TEM sample *ex situ* and also observed nanopores in Ni grains. Such an inhomogeneous nanoporous structure is energetically unfavorable; Ni grain growth by Ostwald ripening will reduce the energy of the system [27]. However, this phenomenon was not observed in the ETEM due to time and temperature constraints.

Additionally, in bulk samples, in contrast to the present observations, interfacial voids are formed between Ni grains and the YSZ matrix on reduction, suggesting that the lower final reduction temperature (500 °C) used in the ETEM may have prevented the reorganization of Ni. Grahl-Madsen et al. [41] used conductivity measurements to demonstrate that reorganization of Ni occurs during reduction. As the TEM sample is thin (~80 nm), the grains are reduced faster when compared with those in bulk samples and less reorganization occurs, which would also explain the presence of energetically unfavorable nanopores inside Ni grains.

Nanovoids are observed and contact between NiO and YSZ is maintained in the TEM sample, whereas a gap appears at NiO/NiO grain boundaries. As the reaction starts at the NiO/YSZ interfaces, Ni clusters are first created at this point. The Ni phase then grows towards the center of the grain and contact with the YSZ is maintained. At higher temperature, when free surface reaction starts, the volume change is accommodated by nanoporosity and bulk shrinkage of the Ni grain, and voids are created at NiO/NiO grain boundaries, at which there is no crystallographic coherence. For an isothermal reduction carried out at a temperature that is high enough to trigger the surface and interface reactions together, contact is not maintained at the NiO/YSZ interfaces as the reaction is not necessarily initiated at this point (see Fig. 7c, which shows

images acquired from a NiO–YSZ sample reduced at 500 °C inside the ETEM). The agglomeration of Ni clusters in the center of the grain creates a void surrounding the Ni grains. The reduced structure of the Ni grains is therefore highly dependent on the experimental parameters (temperature, gas pressure and surface properties).

Significantly, no influence of the electron beam was observed during reoxidation of Ni for the electron dose used in the present work. Moreover, despite the presence of bend contours in the YSZ, cracks were not observed in the 80-nm-thick specimen, in which NiO grains are able to expand out of the plane (Fig. 4c and e). Similar irregular topography is also observed in bulk samples after reoxidation [3,6,42].

Prolonged isothermal evolution of the microstructure during reduction and reoxidation was not studied in this work. Isothermal experiments at sufficiently high temperatures (350–500 °C) are difficult to make inside the ETEM in its current setup, as the gas cannot be preheated. The only possibility is to heat the sample quickly at the desired temperature after the introduction of the gas. During prolonged isothermal exposure, thermal drift is observed in such experiments, which prevents the acquisition of useable images during the reaction, hence the choice of a temperature ramp.

4.4. Redox instability

The observed *in situ* redox cycle is clearly irreversible (compare Figs. 2a, 3f, 4d.1 and d.2). Porosity in the reoxidized structure results in the formation of NiO grains that occupy a larger volume than that of the dense as-sintered grains (Fig. 4c–e), as a result of unbalanced oxidation mass transport. The creation and the movement of bend contours [43] in the YSZ at temperatures higher than 450 °C (once the Ni nanovoids are completely filled by NiO) were observed. We believe this to indicate strongly that NiO expansion during a redox cycle causes this stress in YSZ, rather than being a thermal stress effect (Fig. 3f and Supplementary Video S3).

The stresses that are observed in the YSZ phase (Fig. 3f) will accumulate over successive redox cycles [3], resulting in the cracking of the YSZ phase of the anode and the electrolyte and decreasing the performance of the cell [4]. Coalescence and sintering of Ni grains was not observed during *in situ* reduction, presumably in part due to the relatively low temperature to which the sample was exposed and the relatively short duration of the experiments in the ETEM. However, Ni coarsening is known to occur during SOFC operation and to be partly responsible for the irreversibility of the anode microstructure during a redox cycle [44].

5. Conclusion

ETEM observations and density functional theory calculations are in good agreement. Both demonstrate that the transfer of oxygen from NiO to YSZ, and thus the creation of NiO oxygen vacancies, activates the reduction reaction at the NiO/YSZ interface by the creation of hydrogen adsorption sites (Ni atoms surrounding oxygen vacancies).

The formation of a porous structure during *in situ* reoxidation, due to imbalanced mass transport between outward Ni diffusion and inward oxygen diffusion in oxidizing Ni grains, accounts for the redox instability of the Ni–YSZ anode. The microstructural irreversibility of a redox cycle was clearly demonstrated along with the expansion of Ni and the creation of stress in the YSZ phase.

Based on the present *in situ* ETEM observations, it is possible to propose a design for a redox-resistant fine-grained NiO–YSZ anode, in which dispersed porosity after sintering accommodates redox expansion. If the Ni grains can expand into the porosity, then the stress on the YSZ will be reduced and the formation of cracks in the electrolyte delayed or avoided. Such a fine-grained porous as-sintered NiO–YSZ structure can be obtained by using different strategies, for example by using low sintering temperatures and short sintering times [45] or the addition of specific pore formers. Whereas current research focuses preferentially on coarse microstructures with large pores to accommodate the redox expansion [9,46], this reduces electrochemical performance or necessitates adding a non-redox anode functional layer for sufficient electrochemical activity. A fine microstructure with well-dispersed pores, on the other hand, appears to be an alternative promising way to produce efficient Ni-based anodes with improved redox tolerance and thus enhance the durability of this technology.

This work lays the foundations for further *in situ* SOFC characterization by ETEM, with the ultimate objective being to observe a complete cell during operation inside a TEM to understand the degradation mechanisms. Even if electron beam and sample geometry artifacts must be taken into account while analyzing data, ETEM characterization can yield unique information in the scope of catalysis, corrosion and solid–gas reactions in general.

Appendix A. Supplementary material

Supplementary data associated with this article can be found, in the online version, at doi:10.1016/j.actamat.2010.04.019.

References

[1] Singhal SC, Kendall K. High temperature solid oxide fuel cell–fundamentals, design and applications. Oxford: Elsevier; 2003.
[2] Minh NQ. J Am Ceram Soc 1993;76:563.
[3] Faes A, Nakajo A, Hessler-Wyser A, Dubois D, Brisse A, Modena S, et al. J Power Sources 2009;193:55.
[4] Waldbillig D, Wood A, Ivey DG. J Power Sources 2005;145:206.
[5] Cassidy M, Lindsay G, Kendall K. J Power Sources 1996;61:189.
[6] Klemensø T, Appel CC, Mogensen M. Electrochem Solid-State Lett 2006:9.

[7] Klemensø T, Chung C, Larsen PH, Mogensen M. J Electrochem Soc 2005:152.
[8] Malzbender J, Wessel E, Steinbrech RW. Solid State Ionics 2005;176:2201.
[9] Waldbillig D, Wood A, Ivey DG. Solid State Ionics 2005;176:847.
[10] Sarantaridis D, Chater RJ, Atkinson A. J Electrochem Soc 2008:155.
[11] Hansen PL, Wagner JB, Helveg S, Rostrup-Nielsen JR, Clausen BS, Topsøe H. Science 2002;295:2053.
[12] Hofmann S, Sharma R, Wirth CT, Cervantes-Sodi F, Ducati C, Kasama T, et al. Nat Mater 2008;7:372.
[13] Sharma R. Microsc Res Technol 2009;72:144.
[14] Hansen TW, Wagner JB, Jinschek JR, Dunin-Borkowski RE. Microsc Microanal 2009;15:714.
[15] Boyes ED, Gai PL. Ultramicroscopy 1997;67:219.
[16] Hansen PL, Helveg S, Datye AK. Adv Catal 2006;50:77.
[17] Stadelmann P. JEMS; 2004.
[18] Alicona®. MeX™; 2009.
[19] Giannozzi P, Baroni S, Bonini N, Calandra M, Car R, Cavazzoni C, et al. J Phys-Condens Matter 2009;21:395502.
[20] Perdew JP, Burke K, Ernzerhof M. Phys Rev Lett 1996;77:3865.
[21] Vanderbilt D. Phys Rev B 1990;41:7892.
[22] Xia X, Oldman R, Catlow R. Chem Mater 2009;21:3576.
[23] Henkelman G, Uberuaga BP, Jónsson H. J Chem Phys 2000;113:9901.
[24] Dickey EC, Dravid VP, Nellist PD, Wallis DJ, Pennycook SJ, Revcolevschi A. Microsc Microanal 1997;3:443.
[25] Buckett MI, Marks LD. Surf Sci 1990;232:353.
[26] Little JA, Evans JW, Westmacott KH. Metall Trans B 1980;11:519.
[27] Simwonis D, Tietz F, Stver D. Solid State Ionics 2000;132:241.
[28] Faes A, Hessler-Wyser A, Presvytes D, Vayenas CG, Van herle J. Fuel Cells 2009;9:841.
[29] Wagner T, Kirchheim R, Rühle M. Acta Metall Mater 1995;43:1053.
[30] Shishkin M, Ziegler T. J Phys Chem C 2008;112:19662.
[31] Bonvalot-Dubois B, Dhalenne G, Berthon J, Revcolevschi A, Rapp RA. J Am Ceram Soc 1988;71:296.
[32] Rodriguez JA, Hanson JC, Frenkel AI, Kim JY, Perez M. J Am Chem Soc 2002;124:346.
[33] Richardson JT, Scates R, Twigg MV. Appl Catal, A 2003;246:137.
[34] Furstenau RP, McDougall G, Langell MA. Surf Sci 1985;150:55.
[35] Atkinson A. Rev Mod Phys 1985;57:437.
[36] Atkinson A, Moon DP, Smart DW, Taylor RI. J Mater Sci 1986;21:1747.
[37] Atkinson A, Smart DW. J Electrochem Soc 1988;135:2886.
[38] Mayer J, Giannuzzi LA, Kamino T, Michael J. MRS Bull 2007;32:400.
[39] Tolk NH, Bucksbaum P, Gershenfeld N, Kraus JS, Morris RJ, Murnick DE, et al. Nucl Inst Methods Phys Res, B 1984;2:457.
[40] Su DS, Wieske M, Beckmann E, Blume A, Mestl G, Schlögl R. Catal Lett 2001;75:81.
[41] Grahl-Madsen L, Larsen PH, Bonanos N, Engell J, Linderoth S. J Mater Sci 2006;41:1097.
[42] Sarantaridis D, Atkinson A. Fuel Cells 2007;7:246.
[43] Williams DB, Carter CB. Transmission electron microscopy, a text book for materials science. New-York: Plenum Press; 1996.
[44] Klemensoe T. Relationships between structure and performance of SOFC anodes. Risoe National Laboratory, vol. PhD. Risoe: Technical University of Danemark; 2005.
[45] Fouquet D, Müller AC, Weber A, Ivers-Tiffée E. Ionics 2002;1862–0760:103.
[46] Waldbillig D, Wood A, Ivey DG. J Electrochem Soc 2007:154.